applied optics

Research on the degradation of lightweight mirror surface accuracy

Pingwei Zhou,[1,2,*] Kejun Wang,[1] Changxiang Yan,[1] and Xiaohui Zhang[1]

[1]Changchun Institute of Optics, Fine Mechanics and Physics, Chinese Academy of Sciences, Changchun 130033, China
[2]University of Chinese Academy of Sciences, Beijing 100039, China
*Corresponding author: npuzhoupw@163.com

Received 11 June 2018; revised 7 August 2018; accepted 13 August 2018; posted 15 August 2018 (Doc. ID 334881); published 12 September 2018

The vibration test is one of many tests that space telescopes endure to ensure that functionality is not impaired by severe launch. Telescopes undergo detailed measurements, including mirror surface accuracy measurements. Due to the design shortcomings, degradation of lightweight mirror surface accuracy may exceed the design error budget at times. In this paper, we demonstrate a method to determine the cause of the degradation. By using inertia relief, the influence functions were obtained, and structural deformation was derived from finite element analysis. Based on the structural deformation, we found that the back frame of the telescope had insufficient torsional and bending stiffness. With the indicated need for higher stiffness, the rigidity of the back frame was improved. In addition, high- and low-temperature cycling was used to reduce residual stresses that cause high-frequency distortion. The new vibration test verified the mechanical safety and optical stability of the improved structure. The surface accuracy measured by an optical interferometer was maintained at 0.015 wave within the design error budget.

OCIS codes: (240.6700) Surfaces; (220.4840) Testing; (350.4600) Optical engineering; (350.6090) Space optics.

https://doi.org/10.1364/AO.57.007758

1. INTRODUCTION

Astronomical and Earth observations performed using space telescopes have become increasingly popular in recent years. Space observation has many advantages, including avoidance of the effects of weather and image fluctuations due to atmospheric flow. It also enables multi-spectral detection, which offers more information than Earth-based observations [1]. However, space telescopes must be weight-constrained and be able to resist exceptional conditions, such as launch, temperature changes, and gravity loading during assembly [2]. Of all these, the structural load environment is the most severe. This environment is a combination of quasi-static loads, low- and high-frequency dynamic loads, and shock loads. Quasi-static loads and low-frequency dynamic loads are due to acceleration of the launch vehicle, steering, and engine transients. High-frequency dynamic loads are predominantly of acoustic origin, which are most severe at the stage of lift-off. To verify and prove that functionality is not impaired by severe launch, vibration tests have to been conducted [3]. In particular, bolt slips or adhesive breakage can be detected by modal sweep. During the vibration test, accelerometers and gauges attached to space telescopes are used to detect the structural responses and mechanical stresses, respectively. After that, the telescopes undergo detailed measurements, including mirror surface accuracy measurement and relative angle measurements using an optical interferometer and theodolite, respectively.

Residual stresses can be defined as those stresses existing within a body in the absence of external loading or thermal gradients. Residual stresses can be present in any mechanical structural due to many causes, including the manufacturing process, localized yielding of the material, and differential expansion. While stress due to external loads can be calculated with a degree of accuracy, residual stresses are difficult to measure and calculate or predict. For more stable dimensions, the heat treatment [4] and resonant vibration [5–7] are often used to reduce residual stresses. If residual stresses of the space telescope have not been reduced to a much lower level, degradation of mirror surface accuracy may take place after vibration tests.

When degradation is too large or exceeds the design error budget, the causes should be determined, and structural optimization should be carried out. However, this process heavily depends on the experience of the telescope designer, which can be time consuming. In this study, we demonstrate a method to identify the cause of degradation. First, the difference of two measured images was extracted by subtraction [8] after alignment and scaling. Second, the degradation was decomposed [9], and also structural deformation was derived from the finite element analysis (FEA) using inertial relief. Based on the structural deformation, we found that the back frame of the telescope had insufficient torsional and bending stiffness. With the indicated need for higher stiffness, the back frame

was improved. Last, high- and low-temperature cycling was performed to reduce residual stresses. The mechanical safety and optical stability of the improved structure were verified by the new vibration test.

2. MIRROR AND SUPPORT CONFIGURATION

The ultra-lightweight space telescope, as shown in Fig. 1, is an under-construction Chinese science project, which is planned for launch in 2020. Since the end of 2016, the design, manufacturing, assembly, and tests of this telescope have been started by Changchun Institute of Optics, Fine Mechanics and Physics (CIOMP). It is composed of a front frame, trusses, back frame, and mirror subsystems, which adopt an off-axis, three-mirror optical system. As the total weight of the telescope is limited to 45 Kg, every single component of the space telescope has been of lightweight design. The primary mirror is the heaviest component in the telescope. In this study, a partially closed-back, monolithic, SiC primary mirror configuration [10] is examined. Some advantages of the partially closed-back design include higher mirror flexural rigidity relative to open-back designs and fabrication simplicity relative to built-up configurations. The aperture is 0.45 m, the radius of curvature is 1.6 m, the supporting radius is 0.12 m, the depth is 0.045 m, and the mass is 4.1 kg. The triangular isogrid pattern has a 0.03 m inscribed circle diameter. The mirror is supported by three flexures through the supporting holes located on its back, as shown in Fig. 1. To further reduce the self-weight surface distortion, each semi-kinematic flexure is designed to take a third of the mirror's weight. The three Invar sleeves are bonded to the internal surface of supporting holes by using an epoxy adhesive (GHJ-01(Z)) in a 120° interval for improving thermal stability. The monolithic flexure is attached to the sleeves and back frame by screws, respectively. It is convenient for testing and aligning space optical systems, when the mirror's optical axis is perpendicular to gravity direction. Also, ground testing with the optical axes horizontal can result in less distortion than in the vertical orientation [11]. As the primary mirror is aspheric, a null lens is used for measuring with an optical interferometer. As the primary mirror subsystem verification testing has been performed previously, the vibration test is conducted to verify the system performance. So before and after the vibration test, the primary mirror surface accuracy was measured with the back frame attached and its optical axis horizontal.

3. EXTRACT THE DIFFERENCE OF TWO MEASUREMENTS

Fig. 2(a) represents measured surface accuracy before the vibration test with piston, tilt, and focus Zernike terms removed. Because of the off-axis optical system, part of the light source is obscured by the front frame. This measured result is comprised mostly of fabrication error and deflection under self-weight. The decomposition using 37-term Zernike polynomials fit [12] is shown in Fig. 2(b). It is found that the Zernike term Z5 (primary astigmatism at 90°) and Z10 (primary trefoil

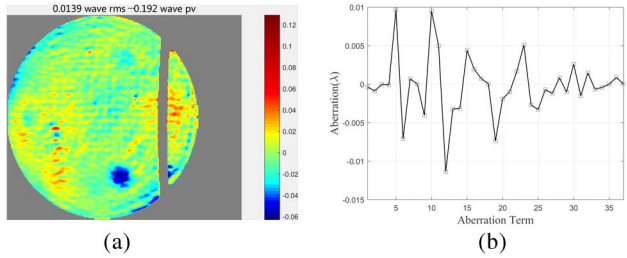

Fig. 2. (a) Measured mirror surface accuracy using optical interferometer before the vibration test. (b) 37-terms fringe Zernike polynomials decomposition. ($\lambda = 632.8$ nm).

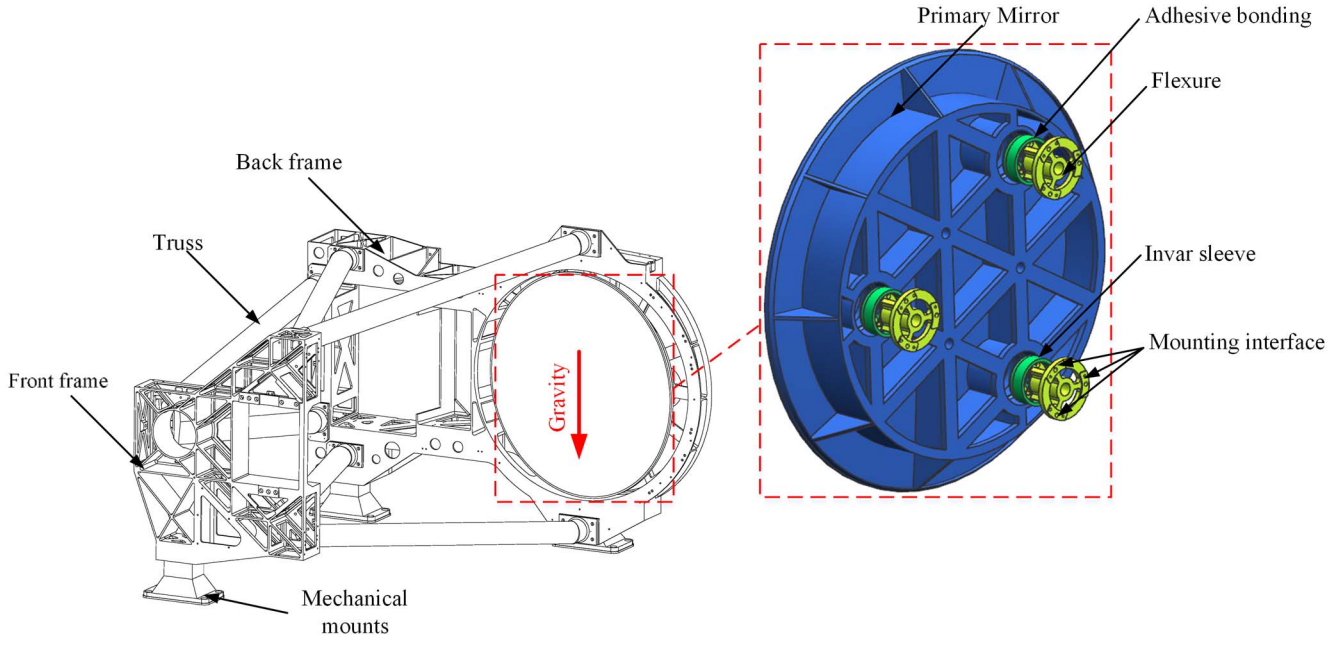

Fig. 1. Components of the space telescope and exploded view of the pre-designed lightweight primary mirror assembly showing the symmetries, invar sleeve, and mounting interface.

at 90°) are relatively high, which is common in horizontally supported mirrors [13]. Measured surface accuracy after the vibration experiment is shown in Fig. 3. In the presented data, piston, tilt, and focus Zernike terms are also removed. Compared with the root mean square (rms) surface distortion before the vibration test, the rms surface distortion after the vibration test degenerated from 0.014 wave to 0.026 wave, which exceeds the design error budget (0.016 wave). Possible concerns have to be found and remedied before the space telescope is launched. In order to extract the difference of two measurements, the first set of interferometric data should be subtracted from the second set of interferometric data. Due to misalignment of the interferometer and change in the radius of the primary mirror in pre- and post-testing, the image size and position at the charge-coupled device (CCD) are different. The center coordinates of first set of interferometric data are located at x 127 and y 245, and the size is 205×251. Accordingly, the center coordinates of the second set of interferometric data are located at x 124 and y 245, and the size is 215×261. So the two sets of interferometric data are aligned and scaled to the same size, 204×250, using bilinear interpolation. Figure 4 shows the difference in two measurements in which the Zernike term Z10 becomes remarkably higher than other Zernike terms.

In order to resolve the high-frequency contribution to degradation of mirror surface accuracy, low-frequency distortion is removed using a 37-term fringe Zernike fit, yielding a high-frequency mean variance of 0.016 wave rms, as shown in Fig. 5(b). Based on the previous experience, this high-frequency deformation is due mainly to the vibration stress relief in the structure and adhesive. Usually, the excessive local deformation

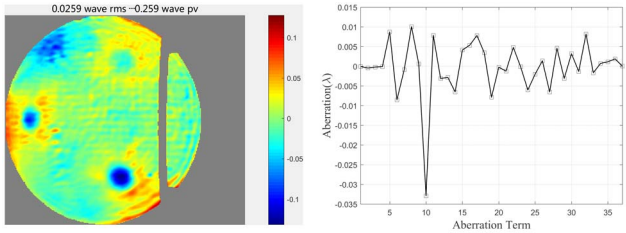

Fig. 3. (a) Measured mirror surface accuracy using optical interferometer after the vibration test. (b) 37-terms fringe Zernike polynomials decomposition. ($\lambda = 632.8$ nm).

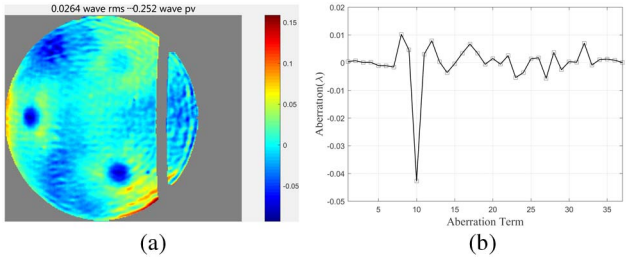

Fig. 4. (a) Degradation of mirror surface accuracy before and after the vibration test. (b) 37-terms fringe Zernike polynomials decomposition.

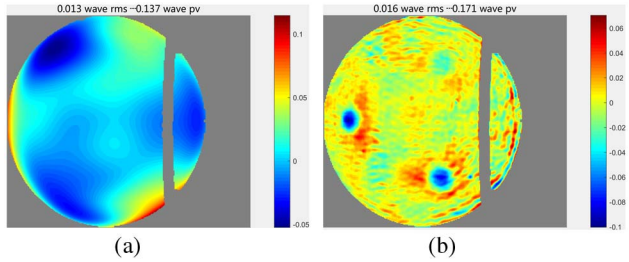

Fig. 5. (a) 37-terms fringe Zernike polynomials decomposition of the degradation. (b) Residual after fit, which includes high-frequency distortion.

at the three supports is due to the local induced stress. As the primary mirror subsystem verification testing has been performed previously, the residual stress can be present only in the frames and trusses. Therefore, the high-frequency distortion can be compensated for by performing high- and low-temperature cycling on the frames and trusses after removing the primary mirror subsystem. As the trusses of the telescope have a relatively simple structure, the possibility of structural deformation is small. In addition, after the vibration test, the relative angle between the primary mirror and the back frame has been measured to be 15″ using theodolite (Leica TM5100A). The measurement result indicates that the vibration test has caused great structural deformation in the back frame. When the back frame has structural deformation, external loads will be transferred to the primary mirror through the mounting interface, as shown in Fig. 1. This external loads can result in low-frequency distortion. So determining the cause of degradation of mirror surface accuracy turns into identifying the cause of structural deformation in the back frame. By improving the rigidity of the back frame, the low-frequency distortion can be compensated.

4. INFLUENCE FUNCTIONS

Inertia relief is an advanced option in ANSYS that allows you to simulate unconstrained structures in a static analysis. It gets the FEA model to exactly balance the force difference (applied force minus weight) in a static analysis with acceleration body forces over the whole structure, so that the reaction on the constraint is zero. During analysis, enough constraints are required to prevent free-body translation and rotation (six for a 3D structure). In this paper, inertia relief is used to determine the influence functions of the forces (F_x, F_y, F_z) and moments (M_x, M_y, M_z) along each of the three orthogonal directions at each flexure. The forces (F_x, F_y, F_z) and moments (M_x, M_y, M_z) altogether consist of the external loads. Each influence function represents the effect of one component of the external loads on mirror surface accuracy. The primary mirror assembly without frames and trusses is analyzed as a free-free structure using inertia relief. First, three mass points are established at centers of the three support flexures and on the mounting interface with the back frame. Second, in order to distribute the external load applied at mass points to the support flexures, the multipoint constraint elements rbe3 are created to connect mass points to the nodes on the mounting interface, respectively. Third, the unit force (1 N) and moment (1 N · mm) along three orthogonal directions are applied to each

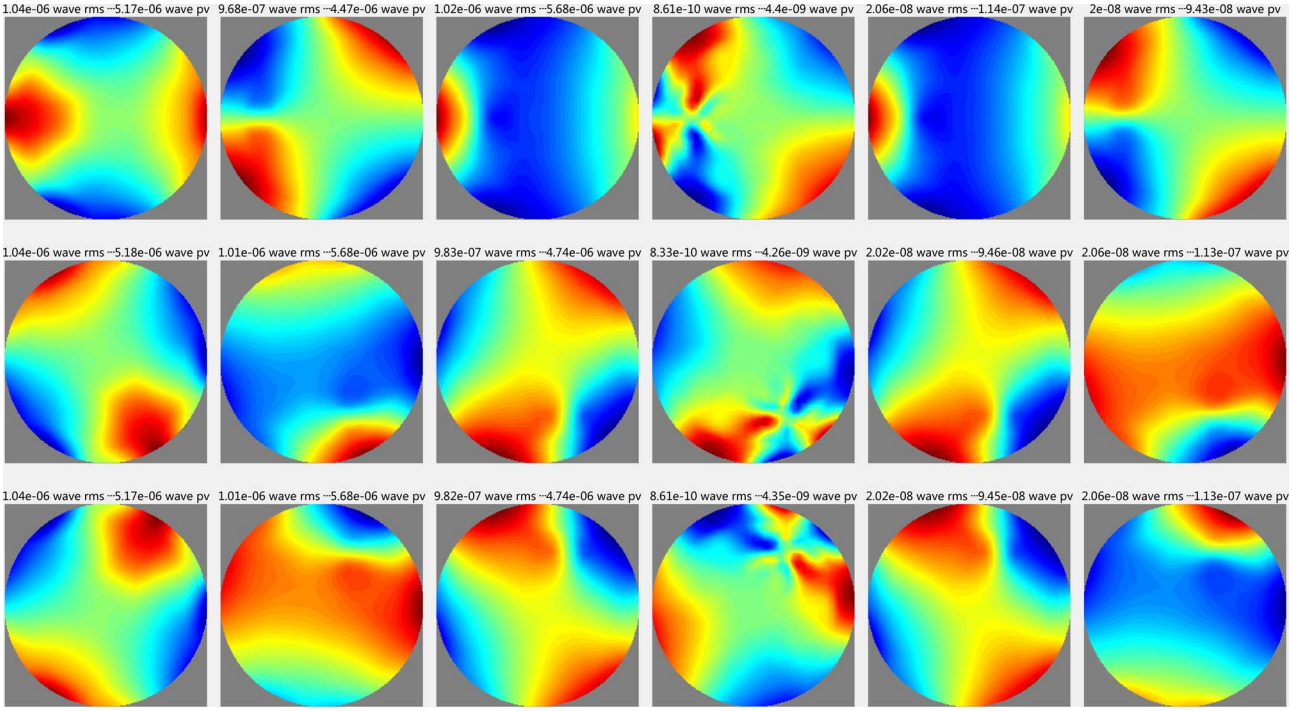

Fig. 6. 18 influence functions derived from the FEA using inertia relief.

of the three mass points, respectively. Last, three arbitrary nodes apart from the nodes on the mounting interface can be selected as constraint points, in which x degree of freedom is prevented at three nodes, y degree of freedom at two nodes, and z degree of freedom at one node. After each analysis, both force reaction and moment reaction are calculated to make sure that they are virtually zero. Figure 6 shows the 18 influence functions in which the piston and tilt are removed. Each row of the figures shown in Fig. 6 represents the unit load applied at one mass point in sequence of F_x, F_y, F_z, M_x, M_y, and M_z.

5. STRUCTURAL DEFORMATION ANALYSIS

With the knowledge of the influence function, one can find the combination of changes in external forces and moments that best approximate any desired degradation of mirror surface accuracy. The 18 influence functions given in Section 4 constitute a characteristic base A, which is used to decompose the degradation of mirror surface accuracy δ_d:

$$\delta_d = A\alpha, \tag{1}$$

with α a set of 18 coefficients corresponding to the external loads. These coefficients are determined by computing the generalized inverse of influence functions base under the condition of force and moment equilibrium:

$$\begin{cases} \alpha = (A^tA)^{-1}A^t\delta_d \\ \text{s.t. } [I_6, I_6, I_6]\alpha = 0 \end{cases}, \tag{2}$$

where I_6 represents the identity matrix of size 6.

Thus, the degradation of mirror surface accuracy actually compensated by the system is

$$\delta_{\text{cor}} = A(A^tA)^{-1}A^t\delta_d. \tag{3}$$

The residual surface distortion after correction is

$$\delta_{\text{res}} = \delta_d - \delta_{\text{cor}}. \tag{4}$$

In fact, the degradation of mirror surface accuracy has been caused by numerous force distributions, part of which are hard to express quantitatively. So the 18 influence functions are able to compensate only some low-frequency distortion. The residual rms after compensation is 0.0074 wave, as shown in Fig. 7(a), which accounts for half of that shown in Fig. 5. It can be seen that the Zernike term Z10 (primary trefoil at 90°) has been compensated for, and the residual aberrations are evenly distributed. After compensation, the surface distortion is within the design error budget.

Table 1 shows the solved external loads acting on the primary mirror assembly using Eq. (4). The maxima of force and moment are 38N and 1203.7 N·mm. Then the solved external loads are applied back to the three mass points accordingly to obtain structural deformation, as shown in Fig. 8. It can be seen that the structural deformation is mostly overall rotation and local bending. From the structural deformation, it was

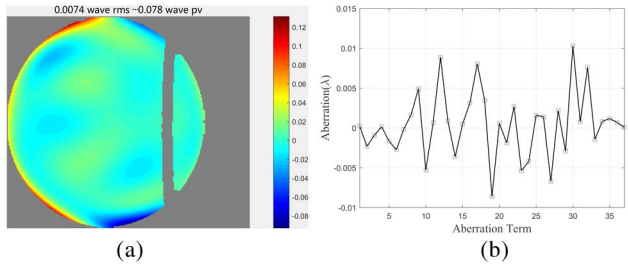

Fig. 7. (a) Residual after compensation. (b) 37-terms fringe Zernike polynomials decomposition.

Table 1. List of the Solved External Loads

Related Mass Points	$F_x(N)$	$F_y(N)$	$F_z(N)$	M_x (N · mm)	M_y (N · mm)	M_z (N · mm)
1#	4.5	−30.1	15.9	16.1	−874.6	−608.7
2#	−2.8	14.9	22.3	−16.8	−329.1	177.6
3#	−1.7	15.2	−38.2	0.7	1203.7	431.1

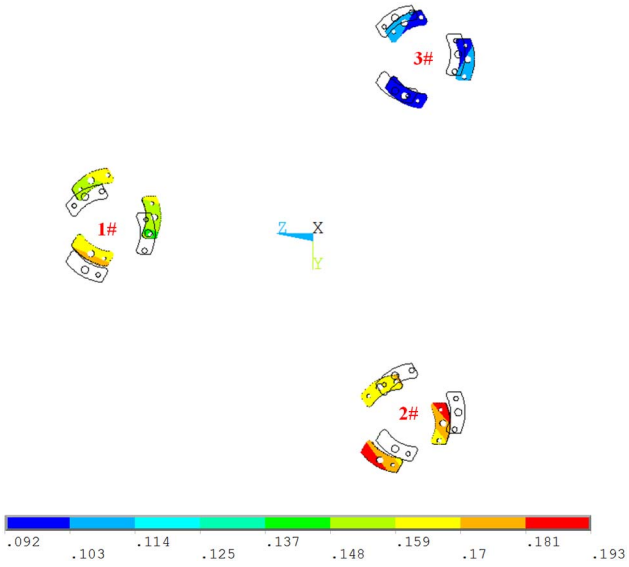

Fig. 8. Structural deformation (mm) of mounting interface resulting from vibration test. For clearness, the mass points and rbe3 elements have been masked.

concluded that the back frame has insufficient torsional and bending stiffness. With the indicated need for higher stiffness, the rigidity of the back frame was improved. Furthermore, high- and low-temperature cycling in the range 15°C–55°C was used to release the internal stresses that cause high-frequency deflection. Last, several new vibration tests verified the mechanical safety and optical stability of the improved structure. Measured surface accuracy, as shown in Fig. 9, by an optical interferometer was maintained at 0.015 wave within the design error budget.

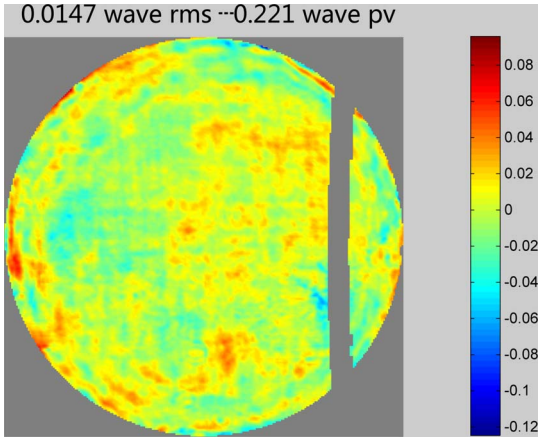

Fig. 9. Measured mirror surface accuracy using optical interferometer after structure improvement and high- and low-temperature cycling.

6. CONCLUSION

This paper presented a method to identify the cause of degradation of lightweight mirror surface accuracy. In order to extract the difference before and after vibration tests, two sets of interferometric data were aligned and scaled to the same size, 204 × 250, using bilinear interpolation. Degradation of mirror surface accuracy includes high-frequency distortion and lower-frequency distortion, which can be expressed by fringe Zernike polynomials. By using inertial relief, the 18 influence functions have been obtained and used to decompose the low-frequency distortion. After compensation, the surface distortion was within the design error budget. In order to obtain the structural deformation of the back frame, the solved external loads have been applied back to the three mass points accordingly. From the structural deformation, it was concluded that the back frame has insufficient torsional and bending stiffness. With the indicated need for higher stiffness, the rigidity of the back frame has been improved. Furthermore, high- and low-temperature cycling was used to release the internal stress that causes high -frequency deflection. Last, several new vibration tests verified the mechanical safety and optical stability of the improved structure. The figure error measured by an optical interferometer was maintained at 0.015 wave within the design error budget.

Funding. National Natural Science Foundation of China (NSFC) (11703027, 61705223).

REFERENCES

1. M. Kotani, T. Imai, H. Katayama, H. Kaneda, T. Nakagawa, and K. Enya, "Quality evaluation of spaceborne SiC mirrors (I): analytical examination of the effects on mirror accuracy by variation in the thermal expansion property of the mirror surface," Appl. Opt. **52**, 4797–4805 (2013).
2. P. Bely, *The Design and Construction of Large Optical Telescopes* (Springer, 2003), pp. 1–28.
3. H. Kihm, H.-S. Yang, I. K. Moon, J.-H. Yeon, S.-H. Lee, and Y.-W. Lee, "Adjustable bipod flexures for mounting mirrors in a space telescope," Appl. Opt. **51**, 7776–7783 (2012).
4. W. Li, S. Li, J. Liu, A. Zhang, Y. Zhou, Q. Wei, and Y. Shi, "Effect of heat treatment on AlSi10Mg alloy fabricated by selective laser melting: microstructure evolution, mechanical properties and fracture mechanism," Mater. Sci. Eng. A **663**, 116–125 (2016).
5. R. Dawson and D. G. Moffat, "Vibratory stress relief: a fundamental study of its effectiveness," J. Eng. Mater. Technol. **102**, 169–176 (1980).
6. D. Rao, D. Wang, L. Chen, and C. Ni, "The effectiveness evaluation of 314L stainless steel vibratory stress relief by dynamic stress," Int. J. Fatigue **29**, 192–196 (2007).
7. S. Mohanty, M. Arivarasu, N. Arivazhagan, and K. P. Prabhakar, "The residual stress distribution of CO_2 laser beam welded AISI 316 austenitic stainless steel and the effect of vibratory stress relief," Mater. Sci. Eng. A **703**, 227–235 (2017).
8. E. E. Bloemhof, J. C. Lam, V. A. Feria, and Z. Chang, "Extracting the zero-gravity surface figure of a mirror through multiple clockings in a flightlike hexapod mount," Appl. Opt. **48**, 4239–4245 (2009).
9. M. Laslandes, C. Hourtoule, E. Hugot, M. Ferrari, C. Lopez, C. Devilliers, and F. Chazallet, "Space active optics: performance of a deformable mirror for in-situ wave-front correction in space telescopes," Proc. SPIE **8442**, 844220 (2012).

10. E. Sein, Y. Toulemont, J. Breysse, P. Deny, D. Chambure, T. Nakagawa, and M. Hirabayashi, "A new generation of large SiC telescopes for space applications," Proc. SPIE **5528**, 83 (2004).
11. R. W. Besuner, K. P. Chow, S. E. Kendrick, and S. Streetman, "Selective reinforcement of a 2m-class lightweight mirror for horizontal beam optical testing," Proc. SPIE **7018**, 701816 (2008).
12. D. Malacara, "Zernike polynomials and wavefront fitting," in *Optical Shop Testing* (Wiley, 2007), pp. 298–545.
13. C. Y. Chan, Y. C. Chen, S. T. Chang, T. M. Huang, and M. Y. Hsu, "Study of bonding positions of isostatic mounts on a lightweight primary mirror," Proc. SPIE **8516**, 85160M (2012).